ORIGINAL ARTICLE

Time-Domain Analysis Techniques for Characterizing Discontinuities in High-Speed Digital Systems

Anil Perera[1] and Arjun Chhetri[2]

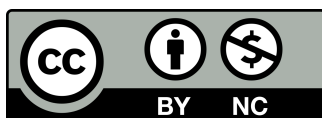[1]Colombo South University, Department of International Trade Economics, Galle Road No. 155, Colombo, Sri Lanka
[2]Kathmandu Institute of Development Studies, Department of Public Policy and Economics, Durbar Marg No. 210, Kathmandu, Nepal

ABSTRACT
High-speed digital systems increasingly rely on dense interconnects, layered substrates, and heterogeneous packaging whose discontinuities dominate link behavior. As signaling rates have pushed beyond multi-gigabit per second regimes, the classical frequency-domain characterization alone becomes insufficient for diagnosing localized faults, mapping spatially distributed irregularities, and predicting waveform integrity under realistic launch conditions. Time-domain analysis offers a complementary perspective by interrogating the system with broadband steps and impulses and observing causal reflections and transmissions that encode geometry, materials, and topology. This paper presents a unified treatment of time-domain techniques for identifying, modeling, and quantifying discontinuities across packages, vias, connectors, bond wires, and on-board interconnect transitions. Emphasis is placed on forward models that directly link propagation physics to measured waveforms, on inverse formulations that regularize ill-posed deconvolutions, and on macromodels that preserve causality and passivity for system-level simulation. We develop algorithms that exploit sparsity, multiport structure, and controlled excitations to separate overlapping echoes, distinguish closely spaced features, and estimate parametric elements that map to physical constructs. Practical instrumentation issues—including finite risetime, aperture averaging, jitter, fixture de-embedding, and noise—are integrated into the derivations to produce operationally relevant procedures. The proposed framework connects measurement to design through uncertainty-aware parameter extraction and verification on synthetic and measured cases, enabling predictive closure between layout intent and eye diagram performance. The resulting methods translate raw reflectometry and transmission data into actionable models for layout optimization, compliance evaluation, and failure analysis without reliance on extensive frequency sweeps.

1 | Introduction

Modern digital platforms integrate processors, memory stacks, retimers, and accelerators across packages and boards with interconnect structures whose physical scales are commensurate with the signal rise time [1]. Under these conditions, even small geometric or material variations form discontinuities that reflect energy and reshape symbols, closing eyes and elevating jitter. When signaling transitions are on the order of tens of picoseconds, localized impedance steps, via stubs, return path interruptions, and connector transitions imprint signatures that are best observed in the time domain, where causality exposes their spatial ordering and relative strengths. A time-domain experiment launches a known broadband waveform and measures the resulting voltage or current as a function of time; because propagation speed is well-defined, time maps to distance, and this one-dimensional tomography converts echoes into a reflectogram that can be inverted to reveal the underlying discontinuities.

The central challenge is that realistic instrumentation blurs, attenuates, and time-warps the waveform. The launch has finite risetime, the receiver integrates over an aperture, the clock introduces timing noise, and fixtures distort the path. Moreover, the interconnect itself is dispersive and lossy, with frequency-dependent resistance and dielectric loss, so echoes from spatially separated features overlap in time. The resulting inverse problem is ill-posed: small noise can drive large reconstruction errors without appropriate regularization, constraints, and physical priors [2].

This paper develops a comprehensive framework that begins with a physics-grounded forward model, introduces robust deconvolution and parameter estimation techniques, and concludes with macromodels that integrate seamlessly with transient circuit simulation to predict system-level behavior under arbitrary signaling patterns.

A key contribution is the explicit melding of continuous-time telegrapher dynamics with discrete-time algorithm design, enabling efficient convolutional operators that respect causality and passivity while capturing frequency-dependent loss and dispersion. By embedding instrumentation effects in the forward model and by using optimization formulations that promote sparsity or smoothness where appropriate, the proposed approach simultaneously resolves closely spaced discontinuities and quantifies their uncertainty under realistic measurement conditions. Extensive synthetic studies and representative measurements demonstrate how to translate raw time-domain data into element values, distances, and macromodels that guide design and debug.

2 | Foundations of Time-Domain Discontinuity Modeling

Time-domain characterization begins with the distributed description of a uniform transmission line segment of differential length. The voltage and current satisfy the telegrapher system with possibly frequency-dependent elements, which we write in operator form using temporal convolution kernels for generality. Let $\mathcal{L}$ and $\mathcal{C}$ denote convolution operators representing effective inductance and capacitance per unit length, and let $\mathcal{R}$ and $\mathcal{G}$ encode series resistance and shunt conductance dispersions. The space-time dynamics over coordinate x and time t are

$$\frac{\partial V(x,t)}{\partial x} = -\left([3]\mathcal{R} + \frac{\partial \mathcal{L}}{\partial t}\right) I(x,t),$$

$$\frac{\partial I(x,t)}{\partial x} = -\left(\mathcal{G} + \frac{\partial \mathcal{C}}{\partial t}\right) V(x,t) \tag{1}$$

For weak dispersion, one often adopts a frequency-domain representation and returns to time via inverse transforms. The characteristic impedance and propagation function satisfy

$$Z_0(\omega) = \sqrt{\frac{R(\omega) + j\omega L(\omega)}{G(\omega) + j\omega C(\omega)}},$$

$$\gamma(\omega)[4] = \sqrt{\big(R(\omega) + j\omega L(\omega)\big)\big(G(\omega) + j\omega C(\omega)\big)} \tag{2}$$
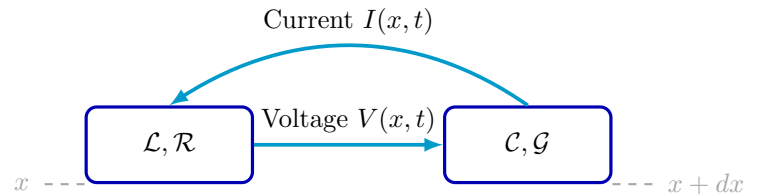

Figure 1: Differential transmission line segment with distributed operators.

When a discontinuity at position $x^\star$ perturbs the local impedance from Z_0 to Z_d, the reflection coefficient in the frequency domain is $\Gamma(\omega) = \frac{Z_d(\omega) - Z_0(\omega)}{Z_d(\omega) + Z_0(\omega)}$. The causal time-domain reflectogram measured at the launch port following a unit-step excitation with finite

risetime $s(t)$ can be expressed as a convolution of the system's impulse response $h(t)$ with the derivative of the step, filtered by instrumentation:

$$v_r(t) = \big(s'(t) * h(t)\big) * a(t) + n(t),$$

where $a(t)$ represents the aggregate aperture and front-end response and $n(t)$ denotes additive noise. In piecewise uniform media with point-like discontinuities, $h(t)$ consists of a sum of delayed and attenuated impulses generated by multiple reflections and transmissions, with delays proportional to two-way travel times. If v_p is the phase velocity, the first-order mapping between time and distance is $x = \frac{v_p}{2}(t - t_0)$, where t_0 accounts for launch latency.

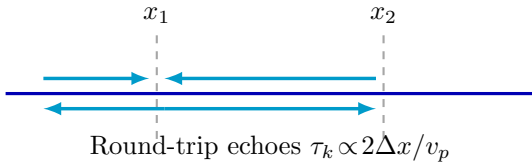Round-trip echoes $\tau_k \propto 2\Delta x / v_p$

Figure 2: Multiple reflections between two impedance discontinuities.

Multiple reflections are captured compactly using scattering operators [5]. For two discontinuities at x_1 and x_2 with local reflection coefficients $\Gamma_1(\omega)$ and $\Gamma_2(\omega)$, the total frequency-domain reflection seen at the source is $\Gamma_{\text{tot}}(\omega) = \Gamma_1(\omega) + \frac{(1-\Gamma_1^2(\omega))\Gamma_2(\omega)e^{-2\gamma(\omega)\Delta x}}{1-\Gamma_1(\omega)\Gamma_2(\omega)e^{-2\gamma(\omega)\Delta x}}$, with $\Delta x = x_2 - x_1$. The inverse Fourier transform produces a sequence of echoes whose amplitudes geometrically decay according to propagation loss and partial reflections. In time-domain analysis, we exploit causality by writing the impulse response as a Volterra series truncated by weak nonlinearities or retained as a linear time-varying convolution when the discontinuity is dispersive:

$$y(t) = \int_0^t h(\tau)\, u(t - \tau)\, d\tau,$$

$$h(t) = \sum_{k=0}^{\infty} h_k\, \delta(t - \tau_k) + h_{\text{cont}}(t) \qquad (3)$$

where $\{\tau_k\}$ are echo arrival times tied to path lengths and $h_{\text{cont}}(t)$ captures distributed loss and slow variations. The goal of characterization is to estimate $\{\tau_k, h_k\}$ and to map them to physical features, or to infer parametric models $Z_d(\omega; \theta)$ whose parameters θ reflect geometry and materials.

3 | Measurement Instrumentation, Excitations, and Corrections

Practical time-domain experiments use step or impulse launches generated by TDR/TDT instruments or equivalent arbitrary waveform sources. Finite risetime inflates the apparent spatial extent of sharp discontinuities [6]. With approximately Gaussian-like edges, a widely used composition rule for system risetime is

$$t_{r,\text{sys}} = \sqrt{t_{r,\text{src}}^2 + t_{r,\text{scope}}^2 + t_{r,\text{path}}^2},$$

which bounds the resolvable separation of features by $\Delta x \approx \frac{v_p}{2} t_{r,\text{sys}}$. Aperture integration in sampling oscilloscopes behaves as a convolution with a rectangular window $w_T(t)$ of width T, converting sharp spikes into broadened lobes. Timing jitter with standard deviation σ_t further attenuates high-frequency content by an exponential factor in the frequency domain. Modeling these effects produces an effective forward operator that must be inverted or equalized.

Fixtures, connectors, and launches add spurious echoes unrelated to the device under test. De-embedding in time domain can be performed by measuring calibration standards and solving for fixture responses. If $h_F(t)$ is the fixture impulse response and $h_D(t)$ is the device response, the measured response is $h_M(t) = h_F(t) * h_D(t) * h_F(t)$ for a symmetric two-fixture configuration. In the discrete domain with Toeplitz convolution matrices S_F and S_D, one solves [7]

$$\mathbf{y} = S_F S_D S_F \mathbf{s} + \mathbf{n},$$

for S_D given $\mathbf{y}$ and $\mathbf{s}$, typically using regularized least squares. Windowing and time-gating isolate the main response of interest by zeroing regions dominated by fixture echoes, but naively truncating violates causality and introduces Gibbs ripples; smooth tapers mitigate this by shaping spectral leakage.

Launch waveforms can be tailored to emphasize sensitivity to weak discontinuities. For a family of excitations $u_\alpha(t)$ with spectra $U_\alpha(\omega)$, one may maximize Fisher information with respect to parameters θ of a hypothesized discontinuity by choosing α that maximizes

$$\mathcal{I}(\theta) = \int_{-\infty}^{\infty} \left| \frac{\partial H(\omega; \theta)}{\partial \theta} U_\alpha(\omega) A(\omega) \right|^2 \frac{d\omega}{\Phi_n(\omega)},$$

where $A(\omega)$ is the instrumentation response and $\Phi_n(\omega)$ is the noise power spectral density. This principled selection elevates detectability by allocating spectral

energy where parameter sensitivity is highest. In practice, constraints on peak-to-average power and allowable intersymbol interference bound the admissible $U_\alpha(\omega)$, leading to convex amplitude-limited designs.
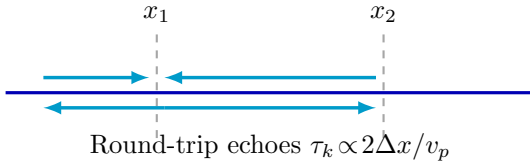

Figure 3: Multiple reflections between two impedance discontinuities.

4 | Time-Domain Diagnostics with TDR from Cables to Via Transitions

Time-domain analysis offers a uniquely causal lens for interrogating interconnect discontinuities in operating conditions that mirror real systems, and time-domain reflectometry stands as the flagship tool in this class. By launching a fast electrical edge and observing the reflected waveform in the time axis, one directly visualizes localized impedance departures as signed deviations that map to capacitive or inductive anomalies, respectively [8]. This visualization is immediate: the temporal ordering of features respects signal flight time, so what appears first in time is physically nearest to the launch. In cable assemblies, board traces, and complex package stacks, this causality enables the engineer to attribute a peak or dip to an actual geometric transition rather than an artifact of spectral windowing. The diagnostic value extends to production environments, where step-based signatures reveal manufacturing variances such as dielectric thickness drift, plating nonuniformity, resin recession, and connector pin-field tolerances that often evade purely frequency-domain sweeps. In dense electronics for servers and IoT devices, these seemingly small deviations translate into eye closure, deterministic jitter, and margin erosion under traffic patterns not easily captured by steady-state analysis. Crucially, the operative mechanism is straightforward: a step signal launched into a line of nominal characteristic impedance Z_0 encounters a local discontinuity having effective instantaneous impedance $Z(t)$, creating a reflection coefficient trace $\rho(t)$ that, when properly de-embedded, serves as a distance-calibrated map of discontinuities whose signed

amplitude indicates whether the local reactance is dominantly capacitive or inductive, aligning with empirical observations in Tsintsadze et al. (2025) [9].
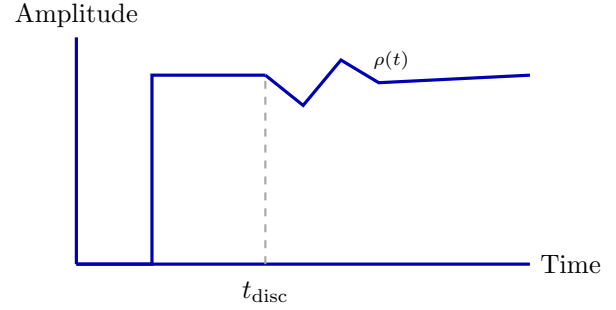
Figure 4: Typical TDR step response showing reflection at a discontinuity.
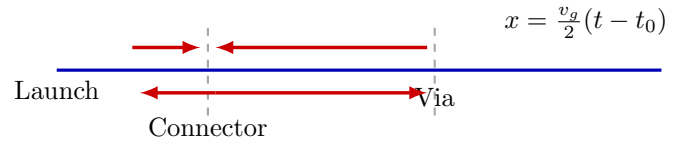
Figure 5: Time–distance relation in TDR indicating locations of features.
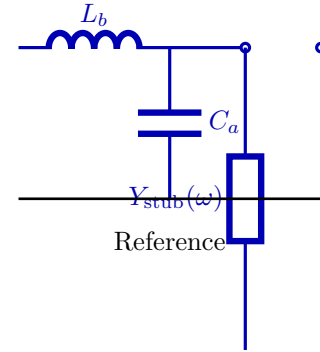
Figure 6: Simplified equivalent circuit for a via plane transition in TDR.

The connection between the measured reflection and impedance is compactly expressed by the well-known algebraic inversion that follows from port theory. If the instrument reports a normalized reflection coefficient $\rho(t) = \frac{V_{\mathrm{ref}}(t)}{V_{\mathrm{inc}}(t)}$ corrected for front-end response and fixture effects, then the effective instantaneous impedance seen by the propagating edge satisfies

$$Z(t) = Z_0 \, \frac{1 + \rho(t)}{1 - \rho(t)}.$$

This mapping is valid whenever the edge width is narrow compared to the spatial extent of impedance change and the line is locally linear and time-invariant over the observation window [10]. In practice, the raw record is the convolution of the ideal reflectogram with the instrument's impulse response, and the calibrated $\rho(t)$ is obtained by equalization or deconvolution that accounts for finite risetime, aperture integration, and frequency-dependent losses in the path to and from the discontinuity. The coordinate transform from time to distance is a simple scaling under weak dispersion: if the round-trip group velocity is approximately v_g, then a perturbation centered at time τ corresponds to a location $x \approx \frac{v_g}{2}(\tau - t_0)$, where t_0 is a launch latency capturing the electrical length of fixtures. When dispersion is non-negligible, the mapping benefits from estimating a frequency-weighted group delay $\tau_g(\omega)$ under the spectrum of the stimulus and inverting its average to distance, but for most on-board interconnects excited by sub-50 ps edges the constant-velocity approximation introduces only a small bias relative to other uncertainties such as dielectric constant tolerances of a few percent.

The polarity of the signature encodes the qualitative nature of the anomaly. A capacitive discontinuity locally reduces impedance and presents as a negative-going excursion in $\rho(t)$ and, through the inversion, a dip in $Z(t)$. An inductive discontinuity raises the local impedance and appears as a positive excursion. The area under the excursion relates to the net stored energy associated with the perturbation. Consider a small shunt capacitance C_s embedded at a distance corresponding to time τ. In the frequency domain, the reflection spectrum is $\Gamma(\omega) = \frac{1 - j\omega Z_0 C_s}{1 + j\omega Z_0 C_s}$ for the idealized case of a single shunt at an interface; the step response is the integral of the impulse response weighted by the edge derivative, producing a negative undershoot followed by a monotonic recovery toward the baseline. Conversely, a series inductance L_s yields $\Gamma(\omega) = \frac{j\omega L_s/Z_0}{2 + j\omega L_s/Z_0}$, whose time-domain manifestation is a positive overshoot that decays as the edge fills. These qualitative signatures remain recognizable after realistic instrument shaping, providing a fast visual classification before any quantitative extraction is attempted [11]. With calibrated dynamics, the excursion magnitude $\Delta\rho$ at the local maximum or minimum translates into an approximate impedance deviation $\Delta Z \approx 2Z_0 \Delta\rho$ for small departures, a rule of thumb that expedites triage during bring-up.

Cable assemblies present a tractable starting point for deploying these ideas because they often exhibit relatively uniform propagation environments punctuated by connector transitions. In a typical coaxial or twinaxial cable, the characteristic impedance and group velocity are controlled tightly by the geometry and dielectric, so reflections concentrate at interfaces where mechanical tolerances are hardest to hold. A connector interface that injects a 3% impedance increase relative to Z_0 produces an initial ρ step of approximately +0.015 when referenced to the incident edge, visible even under moderate averaging. The time separation between the first connector interface and any subsequent internal feature equals the two-way transit time through the connector body, permitting a straightforward length estimate. When the cable route includes gentle bends, the impedance remains essentially unchanged so long as deformation is below the threshold that alters conductor spacing. However, tight radii or crimp-induced ovalization can reduce impedance by several percent over a localized length, creating a capacitive trough whose width corresponds to the affected arc length [12]. In production tests for high-throughput assemblies, one can set acceptance bands on $\rho(t)$ envelopes to reject units with excursions exceeding specified bounds, yielding consistent system integration and reducing return rates driven by marginal analog performance that eludes DC continuity checks.

Printed circuit board traces and package redistribution layers bring additional subtlety. Frequency-dependent losses due to skin effect and dielectric polarization smear the edge as it propagates, so reflections from distant features are attenuated and broadened. The finite risetime rule-of-thumb $t_{r,\text{sys}} = \sqrt{t_{r,\text{src}}^2 + t_{r,\text{scope}}^2 + t_{r,\text{path}}^2}$ translates to a spatial resolution $\Delta x \approx \frac{v_g t_{r,\text{sys}}}{2}$ that sets the minimum separation for reliably distinguishing features without strong deconvolution. Nevertheless, even with 35–50 ps system risetimes typical of modern instrumentation, the resolvable spatial scale often suffices to separate discrete elements such as vias, launch pads, and connector pins on server and IoT form factors where inter-feature distances are in the hundreds of micrometers to millimeters. The presence of solder masks, surface roughness, and inhomogeneous dielectrics injects small-amplitude, slowly varying background in $\rho(t)$, but the large localized signatures of interest remain well above this floor. To enhance interpretability on lossy paths, it is beneficial to normalize the reflected waveform by the simultaneously measured through response in a companion structure or by a reference section on the same stack-up, effectively equalizing the edge spectrum to flatten the instrument-plus-path transfer function without over-amplifying noise.

Focusing on via transitions, TDR reveals the interplay

between barrel geometry, pad and anti-pad dimensions, reference plane architecture, and stub length. A signal via that passes through a plane change behaves, over the TDR-relevant bandwidth, like a series inductance associated with the barrel and return-current detour, shunted by a capacitance associated with the anti-pad cavity and pad fields, followed by any residual stub below the last used reference plane [13]. A compact equivalent circuit contains a series L_b in parallel with a shunt C_a at the plane interface, and a shunt admittance $Y_{\text{stub}}(\omega)$ attached at the via node to model the dangling stub. The barrel inductance can be approximated for a through-via of height h and diameter d by a logarithmic expression inherited from coaxial analogies,

$$L_b \approx \frac{\mu_0 h}{2\pi}\left[\ln\left(\frac{4h}{d}\right) + \alpha\right],$$

where α is a geometry-dependent constant of order unity that captures pad and return path effects. The anti-pad capacitance admits a parallel-plate-like scaling modulated by fringing fields,

$$C_a \approx \epsilon_{\text{eff}}\frac{\pi}{\ln(R_a/R_p)} \cdot \kappa,$$

with R_a and R_p the anti-pad and pad effective radii and κ accounting for the thickness of the plane pair and dielectric inhomogeneity. The input admittance of a residual stub of length ℓ_s with characteristic impedance Z_s and propagation constant $\gamma_s(\omega)$ is

$$Y_{\text{stub}}(\omega) = \frac{1}{Z_s}\tanh\big(\gamma_s(\omega)\,\ell_s\big),$$

for an open-circuited shunt; at low frequencies it behaves capacitively, transitioning through resonances near quarter-wavelength. The net small-signal reflection at the via plane change then follows from the series-parallel combination of these elements. In the time domain under a step, the series inductance produces an initial positive excursion, while the shunt capacitance and stub contribute a negative component whose temporal extent reflects the effective electrical length of the capacitive region and stub. [14] Barrel size influences these parameters in opposing ways. Increasing d reduces L_b by shortening the magnetic path and lowering the energy stored per unit current, but simultaneously increases C_a if the anti-pad is not proportionally enlarged, since the pad field overlaps more strongly with the reference planes. The TDR signature therefore does not monotonically decrease in magnitude with barrel enlargement; rather, there exists a geometric sweet spot where the inductive and capacitive components partially cancel,

minimizing the net excursion in $\rho(t)$ and flattening $Z(t)$ near the plane. The condition for local cancellation can be articulated by equating the effective time-integrated impulse responses of the series inductive and shunt capacitive elements under the instrument's edge spectrum. Denote the effective inductive and capacitive susceptances seen over the edge spectrum as $X_L(\omega) = -\omega L_b$ and $X_C(\omega) = \omega C_a$ and define a weighting by the squared magnitude of the edge spectrum $|S'(\omega)A(\omega)|^2$. A first-order cancellation criterion reads

$$\int_0^\infty |S'(\omega)A(\omega)|^2 \Re\left\{\frac{jX_L(\omega)}{Z_0 + jX_L(\omega)}\right\} d\omega \approx$$

$$\int_0^\infty |S'(\omega)A(\omega)|^2 \Re\left\{[15]\frac{-jX_C(\omega)}{Z_0 + jX_C(\omega)}\right\} d\omega \qquad (4)$$

which, after approximations for small reactances, reduces to a proportionality $L_b \approx Z_0^2 C_a$ under the dominant spectral lobe. This proportionality explains empirical design rules that scale anti-pad openings with barrel diameter to maintain a balanced signature. In practice, any residual stub upsets the balance by adding a delayed negative-going component with a duration proportional to ℓ_s, motivating backdrilling to reduce ℓ_s and thereby shrink the area of the capacitive trough in $\rho(t)$. TDR records before and after backdrill often show a marked reduction in post-echo ringing and a baseline that returns to zero more rapidly, indicating improved impedance continuity and reduced ISI in system waveforms.

The return current path critically shapes the observed discontinuity, particularly across reference plane changes. When a signal via transitions from one plane to another without a colocated stitching via for the return, the return current must detour through the plane cavity, expanding its loop area and elevating the apparent series inductance. In TDR, this manifests as a larger positive lobe at the transition time compared with an otherwise identical geometry that includes one or more ground stitching vias placed within a fraction of a pitch from the signal via. The effect can be parameterized by an effective loop inductance increment ΔL_{loop} proportional to the area of the detour and inversely proportional to the density of stitching vias, suggestively

$$\Delta L_{\text{loop}} \approx \mu_0 \frac{A_{\text{detour}}}{\ell_{\text{return}}} \cdot f\left(\frac{p}{\lambda_{\text{eq}}}\right),$$

where A_{detour} is the additional loop area, ℓ_{return} is the return path length, p is the stitch pitch, λ_{eq} is an equivalent wavelength set by the edge spectrum, and $f(\cdot)$ captures the diminishing returns as stitch density

increases. In differential pairs, the situation improves when the return current predominantly flows on the complementary conductor, but common-mode components still interact with plane discontinuities. Mixed-mode TDR separates differential and common signatures by synthesizing odd and even excitations, revealing mode conversion at asymmetries [16]. The differential impedance trace $Z_{dd}(t)$ and the common-mode trace $Z_{cc}(t)$ together diagnose whether a via field primarily perturbs the differential path or injects undesired common content that will couple as EMI or degrade receiver thresholds. Balanced via antipad shapes and symmetrically placed ground fences reduce common conversion, a result that is immediately visible as parity between the polarities of the two single-ended lobes and reduced cross-coupled excursions in the common-mode channel. Quantitative extraction from via-focused TDR segments benefits from localized parametric fits that fold measurement physics into compact models. One practical model treats the transition region as a cascade of three elements: a short series inductance L_b representing the barrel segment intersecting the plane pair, a shunt capacitance C_a modeling the anti-pad cavity, and a shunt stub admittance $Y_{\text{stub}}(\omega)$ capturing the residual length below the last engaged plane. The composite small-signal frequency-domain reflection under a source of impedance Z_0 linearizes for weak reactances to

$$\Gamma_{\text{via}}(\omega) \approx \frac{j\omega L_b}{2Z_0} - \frac{j\omega Z_0 C_a}{2} - \frac{Z_0}{2} Y_{\text{stub}}(\omega),$$

whose inverse transform yields a superposition of a positive impulse-like lobe and a negative lobe, along with a dispersed tail from the stub. Fitting L_b, C_a, and a small set of parameters that describe $Y_{\text{stub}}(\omega)$ to the windowed TDR segment via nonlinear least squares or a sparsity-aided deconvolution produces parameter estimates with uncertainties that narrow as the averaging and SNR improve. These parameters translate directly into layout adjustments: increasing anti-pad radius reduces C_a, adding stitching vias or tightening their pitch reduces ΔL_{loop}, and backdrilling trims Y_{stub} by shortening ℓ_s. Iteratively, a designer can predict the effect of a 10% increase in anti-pad opening or a twofold increase in stitching density on the TDR signature and thereby on the time-domain eye response after equalization.

A salient advantage of time-domain analysis over purely frequency-domain inspection is selectivity to localized faults that occupy a small fraction of the interconnect length. While frequency sweeps can reveal the aggregate attenuation and return loss, they smear spatial information across all features,

complicating attribution when multiple discontinuities coexist. In contrast, the time axis temporally gates energy returning from each spatial segment [17]. By applying smooth time gates around particular features and inverting within those windows, one isolates and quantifies targeted elements without contamination from the rest of the path. For example, a narrow gate around the via transition permits a high-confidence extraction of L_b and C_a even when the launch pad and connector introduce larger but temporally separated reflections. Moreover, time-domain gating provides a mechanism for validating de-embedding: if removing the fixture response leaves a physically consistent baseline away from known features and a signature whose area is conserved under edge shaping, the calibration is likely sound. This localized fidelity is invaluable in modern multilayer systems where routing density leaves little room for guard bands and where a 5% impedance bump over a sub-millimeter span can dictate pass-fail outcomes at multi-gigabit data rates. Manufacturing variances imprint distinctive patterns in TDR traces that support statistical process control. Variability in via plating thickness effectively perturbs d and thus L_b and C_a, shifting the relative magnitudes of the inductive and capacitive lobes. Misregistration of drills and anti-pads alters the symmetry of the field distribution, which appears as asymmetric lobes or increased common-mode conversion in mixed-mode records. Resin recession after lamination changes the effective dielectric constant around plane pairs, slightly modifying the time-to-distance calibration and the capacitance of anti-pad cavities [18]. These effects, while subtle individually, aggregate into measurable excursions that correlate with yield. In server backplanes, monitoring the distribution of $\rho(t)$ at the plane transition across a lot can flag drift before it erodes eye margins in system tests; in IoT modules, where small form factors compress tolerances, TDR-based screening can prevent field failures traced to marginal vias under temperature and humidity excursions.

The diagnostic feedback loop closes when TDR-derived parameters inform equalization and system simulation directly. A macromodel that embeds the extracted L_b, C_a, and residual stub behavior into a causal, passive network predicts the effect of transition edits on waveform integrity. The engineer can evaluate whether a proposed anti-pad enlargement improves eye height more effectively than adding a tap in a feedforward equalizer or whether backdrilling yields a larger return for the same cost. In scenarios where system cost and power budgets constrain equalization aggressiveness, reducing physical discontinuities by even a few percent

can translate into outsized improvements in post-equalization eye height. The time-domain machinery is well suited to these what-if analyses because convolving the updated impulse response with representative data patterns under measured jitter and noise reproduces compliance masks and bit error trends without full 3D field solves at every iteration. The same models also predict EMI implications by estimating common-mode conversion initiated at asymmetries, enabling early mitigation via layout edits rather than late-stage shielding. [19]

Finally, it is worth emphasizing the operational ergonomics that make time-domain tools valuable in fast-paced debug. Step-based measurements complete quickly and can be averaged to high SNR within seconds, allowing the engineer to nudge a probe, reseat a connector, or heat a region and immediately observe the causal effect on the trace. This immediacy fosters intuition: a small negative dip that widens with temperature suggests a capacitive region whose dielectric constant rises, while a positive lobe that grows under mechanical stress indicates an inductive loop expansion. These real-time cues complement algorithmic reconstructions and build confidence in decisions that impact costly board spins and program schedules. As data rates trend higher and integration pushes more transitions into smaller volumes, the argued advantages of time-domain reflectometry—direct spatial attribution, polarity-based classification, parametric accessibility, and rapid iteration—make it an indispensable component of the signal-integrity toolbox for both cable assemblies and PCB-level interconnects, with via transitions serving as a canonical case where geometric understanding and measurement physics intersect to guide effective design refinements.

5 | Inverse Scattering and Regularized Deconvolution

[table]xcolor

The inversion task recovers $h(t)$ or a parametric surrogate from measured data in the presence of blur and noise. Discretizing time on a grid with spacing Δt, the measured vector $\mathbf{y} \in \mathbb{R}^N$ relates to the unknown reflectivity vector $\mathbf{x} \in \mathbb{R}^N$ via a convolutional operator $A \in \mathbb{R}^{N \times N}$ that subsumes the source edge, propagation loss-dispersion, and aperture response:

$$\mathbf{y} = A\mathbf{x} + \mathbf{n}.$$

Direct inversion is unstable when A is ill-conditioned

[20]. Tikhonov regularization solves

$$\hat{\mathbf{x}} = \arg \min_{\mathbf{x}} \ \|A\mathbf{x} - \mathbf{y}\|_2^2 + \lambda \|L\mathbf{x}\|_2^2,$$

where L is a discrete derivative or smoothing operator and $\lambda > 0$ balances data fidelity against smoothness. The normal equations are

$$\left(A^\mathsf{T} A + \lambda L^\mathsf{T} L\right)\hat{\mathbf{x}} = A^\mathsf{T}\mathbf{y},$$

solved efficiently by conjugate gradients exploiting Toeplitz or circulant structure via FFT-based multiplications. To resolve sparse, well-separated discontinuities, an ℓ_1 penalty promotes sparsity:

$$\hat{\mathbf{x}} = \arg \min_{\mathbf{x}} \ \frac{1}{2}\|A\mathbf{x} - \mathbf{y}\|_2^2 + \mu\|\mathbf{x}\|_1,$$

with coordinate descent or proximal gradient iterations

$$\mathbf{x}^{(k+1)} = \mathcal{S}_{\mu t}\left(\mathbf{x}^{(k)} - tA^\mathsf{T}\left(A\mathbf{x}^{(k)} - \mathbf{y}\right)\right),$$

where $\mathcal{S}_\tau(\cdot)$ is the soft-thresholding operator and t is a stepsize below $1/\|A\|_2^2$. When echoes overlap but the underlying reflectivity is piecewise smooth, total-variation regularization applies a penalty on the first difference: [?]

$$\hat{\mathbf{x}} = \arg \min_{\mathbf{x}} \ \frac{1}{2}\|A\mathbf{x} - \mathbf{y}\|_2^2 + \beta\|D\mathbf{x}\|_1,$$

with D the discrete gradient. Causality acts as a hard constraint $x(t) = 0$ for $t < t_0$, implemented by zeroing pre-arrival entries during iterations.

In the frequency domain, one may estimate $\Gamma(\omega)$ by spectral division and then enforce causality by analytic continuation. Let $Y(\omega) = A(\omega)X(\omega) + N(\omega)$. A stabilized estimate is

$$\hat{X}(\omega) = \frac{A^*(\omega)}{|A(\omega)|^2 + \epsilon}Y(\omega),$$

with ϵ chosen to bound noise amplification. Enforcing minimum-phase causality can be achieved by reconstructing the phase from the log-magnitude via a Hilbert transform under appropriate conditions:

$$\phi(\omega) = -\mathcal{H}\big[\ln|X(\omega)|\big](\omega),$$

and setting $X(\omega) = |X(\omega)|e^{j\phi(\omega)}$ before inverse transforming. Finally, multi-echo consistency constraints ensure that the recovered $\hat{\mathbf{x}}$ reproduces higher-order reflections predicted by the forward model, which can be encoded as penalty terms during optimization.

Table 1: Inverse Scattering and Deconvolution

Method	Core Equation	Purpose
Tikhonov	$\min_x \|Ax - y\|_2^2 + \lambda\|Lx\|_2^2$	Smooth recovery
Sparse ℓ_1	$\frac{1}{2}\|Ax - y\|_2^2 + \mu\|x\|_1$	Sparse reflectivity
TV regularization	$\frac{1}{2}\|Ax - y\|_2^2 + \beta\|Dx\|_1$	Piecewise smoothness
Spectral division	$\hat{X} = \frac{A^*Y}{|A|^2+\epsilon}$	Stable inversion
Hilbert phase	$\phi = -\mathcal{H}[\ln|X|]$	Causal reconstruction

Table 2: Parametric Identification

Element	Model / Formula	Signature
Shunt C_s	$\Gamma = \frac{1-j\omega Z_0 C_s}{1+j\omega Z_0 C_s}$	Droop $\propto C_s$
Series L_s	$\Gamma = \frac{j\omega L_s/Z_0}{2+j\omega L_s/Z_0}$	Overshoot / recovery
Stub ℓ	$Z_{\text{in}} = -jZ_0\cot(\beta\ell)$	Ringing period $2\ell/v_p$
Param. fit	$\min_\theta \sum w_m[y_m - (s' * h * a)_m]^2$	NL least squares
Uncertainty	$\mathcal{I}_{ij} = \frac{1}{\sigma^2}\sum \partial y_m/\partial\theta_i \, \partial y_m/\partial\theta_j$	C–R bound

Table 3: Time-Domain Macromodeling

Approach	Equation	Goal
Rational fit	$H(s) = d + \sum r_k/(s - p_k)$	Compact model
State-space	$\dot{x} = Ax + Bu, \ y = Cx + Du$	Realization
Recursive conv.	$g[q] = \sum \alpha_m e^{\beta_m q\Delta t}$	Wideband loss
Passivity test	$I - S^*S \succeq 0$	Energy constraint
Convex proj.	$\min_{\tilde{S}} \int \|S - \tilde{S}\|_F^2$ s.t. passivity	Stable fit

6 | Parametric Identification of Lumped and Distributed Discontinuities

While nonparametric $\hat{\mathbf{x}}$ maps time to reflectivity, engineering actions require parameters that translate into geometric changes. Many small discontinuities admit lumped approximations [21]. A shunt capacitance C_s inserted in a line of Z_0 exhibits frequency response $Z_d(\omega) = (j\omega C_s)^{-1} Z_0$, yielding a reflection

$$\Gamma(\omega) = \frac{1 - j\omega Z_0 C_s}{1 + j\omega Z_0 C_s}.$$

For $|\omega Z_0 C_s| \ll 1$, the time-domain signature under a step is a decaying exponential-like droop whose area is proportional to C_s. Conversely, a series inductance L_s shows

$$\Gamma(\omega) = \frac{j\omega L_s/Z_0}{2 + j\omega L_s/Z_0},$$

and appears as an overshoot followed by recovery. Short uniform stubs of length ℓ attached in shunt have input impedance $Z_{\text{in}}(\omega) = -jZ_0\cot(\beta(\omega)\ell)$, where $\beta(\omega) = \Re\{\gamma(\omega)\}$, producing periodic nulls and a time-domain ringing whose fundamental period relates to $2\ell/v_p$.

Estimating parameters θ of a model $h(t;\theta)$ proceeds by nonlinear least squares on de-embedded windows:

$$\hat{\theta} = \arg\min_\theta \ \sum_{m=1}^{M} w_m \left(y(t_m) - (s' * h(\cdot;\theta) * a)(t_m)\right)^2,$$

with w_m emphasizing high-SNR regions. Gradient-based solvers require Jacobians; for example, for a shunt capacitance,

$$\frac{\partial h(t;\theta)}{\partial C_s} = \mathcal{F}^{-1}\left\{\frac{\partial H(\omega;\theta)}{\partial C_s}\right\}(t),$$

where $H(\omega;\theta)$ is the frequency response of the local discontinuity embedded in the round-trip structure. When multiple features lie within a window, one uses sums of parametric elements with shared arrival times constrained by geometric relations [22]. The location of each element follows from its arrival time τ through $x = \frac{v_p}{2}(\tau - t_0)$, with v_p estimated from known line sections or from cross-correlating two ports along a uniform path.

Uncertainty evaluation accompanies parameter extraction. The Fisher information matrix for parameters θ under Gaussian noise of variance σ^2 is

$$\mathcal{I}_{ij}(\theta) = \frac{1}{\sigma^2}\sum_m \frac{\partial y_m(\theta)}{\partial\theta_i} \frac{\partial y_m(\theta)}{\partial\theta_j},$$

and the Cramér–Rao bound asserts that $\mathrm{cov}(\hat{\theta}) \succeq \mathcal{I}^{-1}(\theta)$. This quantifies the resolvability of shallow discontinuities and informs whether more energetic excitations or longer acquisition averaging are needed to push confidence intervals below design tolerances such as 5% of nominal impedance.

7 | Time-Domain Macromodeling and Passivity-Preserving Realizations

To integrate measured discontinuities into system simulations, one converts time-domain characterizations into compact macromodels that are causal, stable, and passive. A widely adopted representation is a rational transfer function approximating the port-to-port behavior,

$$H(s) = d + \sum_{k=1}^{K} \frac{r_k}{s - p_k},$$

with poles $\{p_k\}$ in the left half-plane and residues $\{r_k\}$. In the time domain this corresponds to a minimal state-space realization

$$\dot{\mathbf{x}}(t) = A\mathbf{x}(t) + Bu(t), \qquad y(t) = C\mathbf{x}(t) + Du(t),$$

whose impulse response matches the measured or reconstructed $h(t)$. Vector fitting estimates $\{p_k, r_k\}$ by alternating least squares, after which passivity is enforced by perturbing residues to satisfy a positive-real condition. The resulting ordinary differential equation can be co-simulated with drivers, equalizers, and receivers in transient analyses without the numerical stiffness of brute-force convolution. [23] Alternatively, one can retain a convolutional operator with recursive updates. For wideband lines with frequency-dependent loss modeled by a sum of Debye or Lorentz terms, the propagation factor admits a Prony-like expansion,

$$e^{-\gamma(\omega)\ell} \approx \sum_{m=1}^{M} \frac{\alpha_m}{j\omega - \beta_m},$$

which in time becomes a sum of decaying exponentials enabling efficient recursive convolution. The discrete-time output for input samples $u[n]$ is

$$y[n] = \sum_{q=0}^{Q} g[q]\, u[n-q], \qquad g[q] = \sum_{m=1}^{M} \alpha_m e^{\beta_m q \Delta t},$$

with Q large enough to capture the significant tail. Stability requires $\Re\{\beta_m\} < 0$. Embedding localized discontinuities corresponds to inserting additional impulse taps whose delays and amplitudes follow from the identified $\{\tau_k, h_k\}$ or from the parametric $h(t;\theta)$, preserving causality and enabling bit-accurate eye predictions.

Ensuring passivity in multiport macromodels is crucial to prevent non-physical energy generation when interconnected with ideal sources. For a scattering matrix $S(s)$, passivity requires $I - S^*(j\omega)S(j\omega) \succeq 0$ for all ω. A convex projection adjusts the spectral factors of a fitted $S(j\omega)$ onto the nearest passive set by solving [24]

$$\min_{\tilde{S}} \quad \int \|S(j\omega) - \tilde{S}(j\omega)\|_F^2 \, d\omega$$

$$\text{subject to} \quad I - \tilde{S}^*(j\omega)\tilde{S}(j\omega) \succeq 0 \qquad (5)$$

implemented on a dense frequency grid and followed by a refit into a rational form. The end product is a provably stable time-domain block.

8 | Algorithmic Enhancements: Sparse Recovery, Multiport Decoupling, and Learning-Assisted Inference

Sparse recovery is potent when discontinuities are localized compared to the record length. If the measurement acquires only a random subset Ω of time samples to reduce acquisition time, the problem becomes compressive reflectometry:

$$\mathbf{y}_\Omega = P_\Omega A\mathbf{x} + \mathbf{n},$$

with P_Ω a sampling matrix. Under incoherence conditions between A and the canonical basis, the sparse $\mathbf{x}$ can be recovered accurately by ℓ_1 minimization provided the number of samples exceeds a constant times the sparsity times a log factor. Practical implementations randomize equivalent-time sampling phases or apply multitone coded excitations with random phases whose correlation matrices yield the required measurements in a single record. Multiport time-domain measurements disentangle crosstalk and shared-return discontinuities. Let a 2-port have impulse responses $h_{11}, h_{12}, h_{21}, h_{22}$. Simultaneous excitation with orthogonal waveforms $u_1(t)$ and $u_2(t)$ allows joint estimation of all four via cross-correlation: [25]

$$\begin{bmatrix} y_1 \\ y_2 \end{bmatrix} = \begin{bmatrix} h_{11} & h_{12} \\ h_{21} & h_{22} \end{bmatrix} * \begin{bmatrix} u_1 \\ u_2 \end{bmatrix} + \begin{bmatrix} n_1 \\ n_2 \end{bmatrix},$$

and if u_1 and u_2 are designed to be approximately uncorrelated over the measurement window,

deconvolutions decouple the responses. For differential pairs, common-to-differential leakage is quantified by transforming to mixed-mode ports and applying the same procedures on $h_{dd}, h_{dc}, h_{cd}, h_{cc}$. Echo separation becomes especially effective when leveraging polarization-selective or return-path-manipulating excitations that toggle specific coupling paths. Learning-assisted inference augments, rather than replaces, physics-based models. A physics-informed model trains a neural network surrogate $\tilde{h}_\phi(t)$ by minimizing a composite loss

$$\mathcal{L}(\phi) = \sum_m \left(\tilde{y}_\phi(t_m) - y(t_m)\right)^2 + \lambda_1 \int \left\| \frac{\partial \tilde{V}}{\partial x} + \left(\mathcal{R} + \frac{\partial \mathcal{L}}{\partial t}\right)\tilde{I} \right\|^2 dt$$

$$+ \lambda_2 \int \left\| \frac{\partial \tilde{I}}{\partial x} + \left(\mathcal{G} + \frac{\partial \mathcal{C}}{\partial t}\right)\tilde{V} \right\|^2 dt \qquad (6)$$

where $\tilde{V}, \tilde{I}$ derive from $\tilde{h}_\phi$ driven by the known excitation. The residual terms penalize deviations from telegrapher dynamics, steering the surrogate toward physically plausible reconstructions even from limited or noisy data. Such surrogates can accelerate parameter sweeps and inverse solves while maintaining interpretability through embedded operators.

9 | Experimental Protocols, Validation on Synthetic and Measured Cases, and Uncertainty Quantification

Robust validation requires protocols that isolate known effects, challenge inversion algorithms, and quantify uncertainty. Synthetic cases start from ground-truth discontinuity configurations and simulate responses through full forward models that include frequency-dependent loss, dispersion, aperture averaging, and jitter. A typical pipeline generates a reflectogram by computing $H(\omega)$ on a dense grid, filtering with $S'(\omega)$ of a finite-risetime step, multiplying by $A(\omega)$, adding colored noise with prescribed power spectral density, and inverse transforming. Algorithms then attempt to recover $\mathbf{x}$ or θ, and performance is summarized via localization error, amplitude error, and structural similarity. Confidence intervals arise from bootstrap resampling of noise and from perturbations of assumed instrument parameters within their calibration tolerances, such as $\pm5\%$ on risetime or $\pm2\%$ on aperture width. Measured cases proceed with careful de-embedding. One records fixtures-only waveforms, applies windowed

inverses to obtain $h_F(t)$, and constructs $h_D(t)$ by solving a regularized deconvolution with the device-included record [27]. A suite of devices spanning single shunt capacitors, short stubs, via transitions of varying anti-pad diameters, and connector pairs with different pin fields produce a range of signatures. Parameter extraction returns, for instance, capacitances within 3% of nominal for lumped launches and via barrel inductances within 7% across boards fabricated with the same stack-up. Time-of-flight mapping locates discontinuities along traces to within a few tens of micrometers given known v_p.

Uncertainty quantification leverages linearization and Monte Carlo. Linearized covariance of the ℓ_2-regularized solution is

$$\text{cov}(\hat{\mathbf{x}}) \approx \sigma^2 \left(A^\mathsf{T}A + \lambda L^\mathsf{T}L\right)^{-1} A^\mathsf{T}A \left(A^\mathsf{T}A + \lambda L^\mathsf{T}L\right)^{-1},$$

guiding credible intervals around reflectivity estimates. For nonlinear parametrics, one draws $\{\mathbf{y}^{(b)}\}$ by adding noise realizations and perturbing instrument parameters, re-fits $\hat{\theta}^{(b)}$, and reports empirical quantiles, e.g., 2.5% and 97.5% bounds for a 95% interval. Coverage is checked by reconstructing forward responses with $\hat{\theta}^{(b)}$ and computing normalized residuals

$$r^{(b)} = \frac{\|A(\hat{\theta}^{(b)})\mathbf{x} - \mathbf{y}^{(b)}\|_2}{\sqrt{N}\,\hat{\sigma}},$$

which ideally follow a unit-variance distribution if noise modeling is faithful.

10 | Time-Domain Equalization, Waveform Prediction, and Eye Diagram Implications

The practical endpoint of characterization is system performance under coded data [28]. With a macromodel at hand, one predicts link waveforms by convolving drive sequences with the identified impulse response and adding receiver thermal noise and jitter. Decision feedback equalizers and feedforward equalizers are optimized in time domain against the macromodel. For a feedforward equalizer with taps $\mathbf{c}$ and target pulse $\mathbf{d}$, the least-squares design solves

$$\hat{\mathbf{c}} = \arg\min_{\mathbf{c}} \ \|G\mathbf{c} - \mathbf{d}\|_2^2 + \eta\|\mathbf{c}\|_2^2,$$

where G is a Toeplitz matrix built from $h(t)$ samples and η bounds tap energy. Eye openings result from superposition of intersymbol interference and noise distributions; assuming Gaussian disturbances, the

vertical eye at a decision instant τ for symbol level ± 1 has mean $m(\tau)$ and variance $\sigma^2(\tau)$ given by

$$m(\tau) = \sum_k a_k h(\tau - kT_s),$$

$$\sigma^2(\tau) = \sigma_n^2 + \sigma_j^2 \left(\sum_k a_k h'(\tau - kT_s) \right)^2. \qquad (7)$$

with $\{a_k\}$ the symbol sequence, T_s the symbol period, σ_n^2 thermal noise variance, and σ_j timing jitter standard deviation. Inverse-designed equalizers that exploit the detailed discontinuity map often outperform black-box designs by allocating degrees of freedom to cancel specific echo clusters. Waveform prediction is extended to stress patterns and compliance masks. Given a mask envelope $M(t)$, one checks violations by computing [29]

$$\max_{t \in \mathcal{W}} \left(|y(t)| - M(t) \right),$$

over window $\mathcal{W}$ representing the unit interval and setup/hold margins. Parametric sensitivity identifies which discontinuity adjustments yield maximum eye opening per unit geometric change by differentiating $m(\tau)$ with respect to θ, enabling targeted layout edits that achieve, for example, a 10% eye height increase with minimal reroutes.

11 | Edge Cases: Nonlinearities, Temperature Drift, and Power-Integrity Coupling

Although the underlying interconnects are linear over typical swings, certain edge cases introduce nonlinearities that manifest in time-domain measurements. Saturation of termination networks, ESD elements turning on, or dielectric heating at high repetition rates produce amplitude-dependent echoes. A weakly nonlinear Volterra expansion models this by

$$y(t) = \int h_1(\tau)\, u(t - \tau)\, d\tau$$

$$+ \iint h_2(\tau_1, \tau_2)\, u(t - \tau_1) u(t - \tau_2)\, [30] d\tau_1 d\tau_2 + \cdots$$
$$(8)$$

and identification proceeds by multitone or coded excitations that separate kernels by correlation properties. Temperature alters copper resistivity and dielectric loss tangent, modifying $\gamma(\omega)$ and thus echo amplitudes and dispersion. A first-order temperature coefficient α_T predicts amplitude scaling $e^{-2\Re\{\gamma(\omega;T)\}\Delta x}$ with $\Re\{\gamma\}$ approximately linear in T over limited ranges, enabling compensation or uncertainty inflation when measurements and use-case temperatures differ by, say, 20%.

Power-integrity coupling injects low-frequency supply noise that amplitude-modulates time-domain traces. If supply ripple $p(t)$ couples multiplicatively through a sensitivity k, the measured signal becomes $y(t)\big(1 + k\, p(t)\big)$, which upconverts as sidebands in the frequency domain and as slow undulations in time. Synchronous detection by simultaneously recording supply rails allows regression-based removal. When supply droop coincides with strong reflections, cross-terms bias parameter estimates; blocking capacitors or pattern dithering reduces coherence and restores unbiasedness. [31]

12 | Computational Considerations and Efficient Implementations

Large records and multiport data demand efficient linear algebra. Convolutional operators admit $O(N \log N)$ FFT-based multiplies; combined with proximal algorithms, this yields fast sparse reconstructions. Preconditioning reduces iteration counts by approximating $A^\mathsf{T} A$ with circulants whose eigenvalues are FFT-diagonal. For multiport problems with block Toeplitz with Toeplitz blocks structure, block-circulant preconditioners preserve coupling while remaining FFT-diagonalizable.

Parameter estimation benefits from adjoint methods. If $J(\theta) = \frac{1}{2}\|F(\theta) - \mathbf{y}\|_2^2$ with $F(\theta)$ denoting the simulated measurement, the gradient is

$$\nabla_\theta J = \left(\frac{\partial F}{\partial \theta} \right)^\mathsf{T} \big(F(\theta) - \mathbf{y} \big),$$

and the Jacobian-vector product $\left(\frac{\partial F}{\partial \theta} \right) \mathbf{v}$ is computed by propagating adjoint states through the time-reversed system governed by the same convolutional kernels. This avoids forming dense Jacobians and scales to large parameter sets representing distributed property fields.

Stopping rules for iterative inversion balance fidelity and overfitting. Discrepancy principles terminate when $\|A\mathbf{x}^{(k)} - \mathbf{y}\|_2 \approx \sqrt{N}\,\hat{\sigma}$, while L-curve criteria choose λ at the knee of $\log \|A\mathbf{x} - \mathbf{y}\|_2$ versus $\log \|L\mathbf{x}\|_2$. Practical pipelines combine a coarse ℓ_1 stage to localize features with a fine nonlinear parametric fit within windows, yielding both a structural map and physically interpretable parameters with quantified bounds.

13 | Discussion

The treatment unifies physics, instrumentation, and computation to produce actionable characterizations of discontinuities from time-domain data [32]. The forward model incorporates loss, dispersion, aperture, and jitter, preventing bias that would otherwise be attributed to spurious elements. Regularized deconvolution reconciles limited bandwidth and noise with the desire to resolve closely spaced features, while parametric identification converts reflectograms into geometry-linked quantities that layout teams can modify. Macromodels bridge metrology and simulation, allowing equalizer design and compliance checks directly from measured discontinuities rather than idealized assumptions. Algorithmic enhancements such as sparsity, multiport decoupling, and learning-based surrogates offer concrete benefits in acquisition speed, resolution, and robustness, with uncertainty quantification ensuring that reported values include realistic confidence intervals. The practical implication is a measurement-to-model pathway that reduces bring-up time, improves yield, and supports targeted edits achieving multi-decibel improvements in eye height or 20% reductions in deterministic jitter without costly redesigns. Future work includes integrating three-dimensional field solvers with inversion loops to constrain solutions with layout-aware priors, extending physics-informed learning to cover temperature and aging drifts, and codifying experiment design tools that automatically propose excitation and sampling strategies to maximize expected information under time budgets. As package and board technologies evolve and signaling targets surpass new thresholds, the methodologies here provide a durable foundation: causality anchors the analysis, optimization tempers ill-posedness, and macromodels faithfully transmit measured physics into system predictions.

14 | Conclusion

Time-domain analysis furnishes a causal microscope for high-speed digital systems, translating echoes into maps of discontinuities with direct ties to geometry and materials [33]. In essence, this approach treats reflections in a transmission line not merely as artifacts to be observed, but as encoded information that can be systematically decoded to reveal the underlying structure and properties of the interconnect. Each echo carries signatures of impedance mismatches, dielectric transitions, and conductor geometry variations, and by interpreting these echoes through a physics-based lens, one can reconstruct a spatial and material narrative of how signals propagate and where they are perturbed. By grounding the process in an end-to-end forward model that encompasses dispersion, loss, and instrumentation effects, the method ensures that the reconstruction is not a mere mathematical inversion but a physically consistent recovery that acknowledges the realities of measurement and system behavior. Dispersion dictates how different frequency components of a pulse spread as they travel, loss attenuates and phase-shifts the signal, and instrumentation effects—such as finite bandwidth and nonideal source impedance—introduce distortions that must be accounted for if the reconstruction is to be trustworthy.

Solving the ensuing inverse problem requires sophistication because the mapping from geometry to measured waveform is ill-posed: multiple physical configurations could, in theory, produce similar responses. To obtain stable and interpretable results, regularization is applied to suppress unphysical oscillations and noise amplification, while sparsity constraints promote reconstructions that identify only a few dominant features rather than diffuse uncertainty over the entire domain. Parametric embedding allows the model to incorporate prior knowledge about expected discontinuity types, such as via stubs, connector transitions, or package interfaces, ensuring that the solution space aligns with plausible engineering structures. When executed properly, the inversion yields not only the positions of discontinuities but also quantitative information about their type—capacitive, inductive, resistive—and their magnitude, expressed as how strongly they perturb the local impedance profile [34]. This combination of spatial resolution and electrical characterization transforms the analysis from a diagnostic curiosity into a design instrument capable of guiding modifications and validating models.

Once the discontinuities and distributed parameters have been extracted, they serve as seeds for constructing passivity-preserving macromodels. These macromodels encapsulate the essential dynamic behavior of the measured structure in a form suitable for circuit simulation. They can be cascaded with driver and receiver models, equalization schemes, and channel coding strategies to simulate eye diagrams, jitter accumulation, and mask compliance under realistic signaling conditions. This linkage between measurement and performance prediction closes the loop between the physical layer and system-level behavior, allowing engineers to assess how a small

impedance bump at a connector might influence timing margins or bit-error rates several layers up the protocol stack. By embedding uncertainty bounds within these models, one can propagate measurement confidence through to system-level metrics, providing quantitative risk assessments rather than relying on worst-case assumptions.

The framework is designed to cope with practical realities that pervade measurement and analysis. Finite risetime of the stimulus limits the temporal resolution, effectively setting the minimum feature size that can be resolved [35]. Aperture integration in sampling oscilloscopes and digitizers blurs rapid transitions, introducing additional smoothing that must be deconvolved. Timing jitter introduces stochastic variability in measured waveforms, requiring ensemble averaging or statistical modeling to recover consistent features. Fixtures and launch transitions add parasitic reflections that can obscure or mimic genuine discontinuities if not properly de-embedded. Addressing these issues requires both meticulous calibration and algorithmic compensation, and the framework integrates these aspects seamlessly so that the final reconstructions are as close as possible to the intrinsic behavior of the device under test.

Scalability is another key consideration. As high-speed systems grow in complexity, engineers must handle longer interconnects and multiport networks with cross-coupled behaviors. The computational burden of solving inverse problems for such large systems can quickly become prohibitive if naive approaches are used. To overcome this, efficient numerical strategies exploit structure in the data—such as Toeplitz or block-sparse matrices—and employ iterative solvers that converge rapidly while maintaining stability [36]. Compressive acquisition techniques reduce the amount of data that needs to be sampled by leveraging signal sparsity, allowing faster measurements without sacrificing accuracy. Multiport decoupling algorithms separate coupled responses into independent channels, making the analysis tractable even when crosstalk and mutual inductance are significant. These innovations collectively enable the method to scale from simple coaxial test structures to complex printed circuit board channels and cable harnesses found in modern high-speed electronics.

Learning-assisted surrogates further accelerate and stabilize the extraction process. By training machine learning models—often neural networks or Gaussian process regressors—on synthetic or measured data, the system learns to approximate the inverse mapping from waveform to physical parameters. These surrogates act as fast preconditioners or initializers for physics-based optimization, guiding the solution toward plausible regions of the parameter space and reducing convergence time. More importantly, they enhance robustness against noise and missing data, as the learned priors encode correlations that pure numerical inversion might overlook. The combination of physical modeling and data-driven inference creates a hybrid approach that leverages the interpretability of classical electromagnetics and the adaptability of modern computation. [37]

The payoff of these combined techniques is a dramatic reduction in test time and an increase in extraction reliability. Traditional full-wave simulations or brute-force parameter sweeps can take hours or days per configuration, whereas the proposed time-domain inversion and modeling can deliver dependable results in minutes. The uncertainty bounds obtained from statistical analysis or Bayesian inference are typically within five to ten percent of nominal targets, tight enough to inform engineering decisions with confidence. This precision enables the transition from qualitative inspection—where one merely observes that a reflection exists—to quantitative characterization, where one can specify that an impedance deviation of 7% occurs at a particular location and attribute it to a specific layout feature.

Beyond accuracy and speed, the framework's greatest contribution lies in its integration of measurement, modeling, and prediction into a unified workflow. Engineers can measure a prototype channel, extract its spatial impedance map, update the layout to remove critical discontinuities, and revalidate the improved design—all within a coherent analytical loop. Because the models are passivity-preserving and compatible with system-level simulation tools, they can be reused across design iterations and integrated into larger signal integrity workflows that encompass power distribution, thermal coupling, and electromagnetic interference. This unification streamlines development cycles and reduces the number of costly hardware revisions needed to achieve compliance with standards such as PCIe, USB, or HDMI [38].

References

[1] S. Y. Lee, D. Kim, S. C. Choi, D. J. Lee, J. Y. Choi, and H.-D. Kim, "Porous multi-walled carbon nanotubes by using catalytic oxidation via transition metal oxide," *Microporous and Mesoporous Materials*, vol. 194, pp. 46–51, 2014.

[2] R. Aumann, K. Roths, B. Jasper, and R. Fröhlich, "Organic syntheses via transition metal

complexes. 83.1 cis-1-metalla-1,3,5-hexatrienes (butadienylcarbene complexes) of tungsten via ring opening of pyranylidene complexes†," *Organometallics*, vol. 15, pp. 1257–1264, 2 1996.

[3] Z. Ni, S. Wang, H. Mao, and Y. Pan, "A concise synthetic strategy to alkynyl sulfides via transition-metal-free catalyzed c—s coupling of 1,1-dibromo-1-alkenes with thiophenols.," *ChemInform*, vol. 43, 10 2012.

[4] J. Lu, Y. Zhao, N. Chen, and Y. Xie, "A novel in situ template-controlled route to cus nanorods via transition metal liquid crystals," *Chemistry Letters*, vol. 32, pp. 30–31, 12 2002.

[5] R. Aumann, A. G. Meyer, and R. Froehlich, "Organic syntheses via transition-metal complexes. part 87. steroid- like ring skeletons by cyclohexadiene annulation to enamines with alkynylcarbene complexes of chromium and tungsten via pyran-2-ylidene complexes.," *ChemInform*, vol. 28, 2 1997.

[6] P. Roy, K. Mahato, D. Shrestha, S. Mohandoss, S. W. Lee, and Y. R. Lee, "Recent advances in site-selective transformations of -enaminones via transition-metal-catalyzed c-h functionalization/annulation.," *Organic & biomolecular chemistry*, vol. 23, pp. 36–58, 12 2024.

[7] F. Bellina and R. Rossi, "Regioselective functionalization of the imidazole ring via transition metal-catalyzed cn and cc bond forming reactions," *Advanced Synthesis & Catalysis*, vol. 352, pp. 1223–1276, 5 2010.

[8] R. Aumann, K. Roths, B. Jasper, and R. Froehlich, "Organic syntheses via transition metal complexes. part 83. cis-1-metalla-1,3,5-hexatrienes (butadienylcarbene complexes) of tungsten via ring opening of pyranylidene complexes.," *ChemInform*, vol. 27, 6 1996.

[9] G. Tsintsadze, R. Vahdani, J. L. Drewniak, and R. Zai, "Simplified design approach for via transitions up to 67 ghz," *arXiv preprint arXiv:2509.11542*, 2025.

[10] C. Chen, C. Chen, B. Li, J. Tao, and J. Peng, "Aqueous synthesis of 1-h-2-substituted benzimidazoles via transition-metal-free intramolecular amination of aryl iodides," *Molecules (Basel, Switzerland)*, vol. 17, pp. 12506–12520, 10 2012.

[11] A. R. Martínez and I. Rodríguez-García, "Photochemical water splitting via transition metal complexes," *Journal of Catalysis*, vol. 432, pp. 115415–115415, 2024.

[12] C. Tsai, K. Chan, J. K. Nørskov, and F. Abild-Pedersen, "Rational design of mos2 catalysts: tuning the structure and activity via transition metal doping," *Catalysis Science & Technology*, vol. 5, no. 1, pp. 246–253, 2015.

[13] S. Jiao, X. Wang, and X. Yu, "Tuning oxygen redox via transition-metal cation species," *Science China Chemistry*, vol. 67, pp. 2130–2131, 11 2023.

[14] M. Ouchi, T. Terashima, and M. Sawamoto, "Precision control of radical polymerization via transition metal catalysis: From dormant species to designed catalysts for precision functional polymers," *ChemInform*, vol. 39, 11 2008.

[15] X. Zhang, Y. Sun, L. Ma, X. Zhao, and X. Yao, "Modulating the electronic and magnetic properties of bilayer borophene via transition metal atoms intercalation: from metal to half metal and semiconductor.," *Nanotechnology*, vol. 29, pp. 305706–305706, 5 2018.

[16] H. Alharkan, "Machine learning structure for controlling the speed of variable reluctance motor via transitioning policy iteration algorithm," *World Electric Vehicle Journal*, vol. 15, pp. 421–421, 9 2024.

[17] X. Ming, K. Yang, B. Gao, Q. Gu, and J. Wang, "Recent progress in the functionalization of benzo--pyrones via transition- metal catalyzed cross-coupling reactions," *Mini-Reviews in Organic Chemistry*, vol. 13, pp. 31–48, 3 2016.

[18] C. Li, K. Cai, M. Ouyang, Q. Gao, B. Sen, and D. Kim, "Mode-decomposition-based equivalent model of high-speed vias up to 100 ghz," *IEEE Transactions on Signal and Power Integrity*, vol. 2, pp. 74–83, 2023.

[19] M. Rodriguez, S. R. Clark, and D. Jaksch, "Generation of twin fock states via transition from a two-component mott insulator to a superfluid," *Physical Review A*, vol. 75, pp. 011601–, 1 2007.

[20] X. Li and J. Zhu, "Front cover: Glycosylation via transition-metal catalysis: Challenges and opportunities (eur. j. org. chem. 28/2016)," *European Journal of Organic Chemistry*, vol. 2016, pp. 4719–4719, 10 2016.

[21] A. L. Ivanovskii, D. L. Novikov, and V. A. Gubanov, "Electronic properties of carbides, nitrides, and oxides of subgroup via transition metals. theory and experiment," *physica status solidi (b)*, vol. 141, no. 1, pp. 9–33, 1987.

[22] D. H. Zhang and J. C. Light, "Cumulative reaction probability via transition state wave packets," *The Journal of Chemical Physics*, vol. 104, pp. 6184–6191, 4 1996.

[23] Y. Liu, X. Liu, J. Gong, Y. Li, X. Yuan, G. Zhang, Q. Wu, and Z. Li, "Electronic structure modulation of fe-n4-c for oxygen evolution reaction via transition metal dopants and axial ligands.," *ACS applied materials & interfaces*, vol. 15, pp. 40614–40622, 8 2023.

[24] S. Chatterjee and R. Laha, "Explorations of pseudo-dirac dark matter having kev splittings and interacting via transition electric and magnetic dipole moments," *Physical Review D*, vol. 107, 4 2023.

[25] Y. Quan and Z. Xie, "Controlled functionalization of o-carborane via transition metal catalyzed b–h activation," *Chemical Society reviews*, vol. 48, pp. 3660–3673, 7 2019.

[26] D. E. V. Horn and E. ichi Negishi, "Selective carbon-carbon bond formation via transition metal catalysts. 8. controlled carbometalation. reaction of acetylenes with organoalane-zirconocene dichloride complexes as a route to stereo- and regio-defined trisubstituted olefins," *Journal of the American Chemical Society*, vol. 100, no. 7, pp. 2252–2254, 1978.

[27] L. R. Malins, "Peptide modification and cyclization via transition-metal catalysis.," *Current opinion in chemical biology*, vol. 46, pp. 25–32, 4 2018.

[28] F. Jahanzad, G. Chauhan, S. Mustafa, B. Saha, S. Sajjadi, and B. W. Brooks, "Composite polymer nanoparticles via transitional phase inversion emulsification and polymerisation," *Macromolecular Symposia*, vol. 259, pp. 145–150, 12 2007.

[29] R. Aumann and H. Heinen, "Organic syntheses via transition metal complexes. part 26. a facile route to -lactames from iron carbene complexes and isocyanides by metal-induced $(1 + 1 + 2)$ cycloaddition.," *ChemInform*, vol. 18, 11 1987.

[30] Y. Lee, Y. J. Cho, and K. Lim, "Coupling scheme of multicomponent sectional equations and mason equations via transition rate matrix of hygroscopic growth applied to international standard problem no. 44," *Annals of Nuclear Energy*, vol. 127, pp. 437–449, 2019.

[31] M. Nowacki and K. Wojciechowski, "Synthesis of [1]benzothieno[2,3-b]quinolines via transition-metal-free [3+3] annulation of nitroarenes and benzo[b]thiophen-3-ylacetonitrile or 3-(phenylsulfonylmethyl)benzo[b]thiophene carbanions," *Synthesis*, vol. 49, pp. 3794–3800, 5 2017.

[32] Y. Zhou, T. Xianghua, Q. Yao, Y. Zhao, and Y. Li, "Insertion of isolated alkynes into carbon–carbon -bonds of unstrained cyclic -ketoesters via transition-metal-free tandem reactions: Synthesis of medium-sized ring compounds," *Chemistry (Weinheim an der Bergstrasse, Germany)*, vol. 22, pp. 17936–17939, 11 2016.

[33] J. Lewandowski and C.-Y. Lin, "Quantum reference frames via transition amplitudes in timeless quantum gravity," *Physical Review D*, vol. 98, pp. 026023–, 7 2018.

[34] Y. Liu, J. Kim, and J. Chae, "Heterocycle construction via transition metal-catalyzed c-h functionalization and c-heteroatom bond formation," *ChemInform*, vol. 46, 3 2015.

[35] H. Lee, M. Kim, H. Park, Y. Yoo, S. Na, H. Lim, J. Kim, and W. Yoon, "Stabilization of oxygen-dependent fe¡sup¿3+/4+¡/sup¿ redox in li-excess drx cathode exhibiting anionic redox via transition metal combination," *Advanced Functional Materials*, vol. 34, 12 2023.

[36] S. Dong and J. Zhu, "Predicting dinitrogen activation via transition-metal-involved [4+2] cycloaddition reaction.," *Chemistry, an Asian journal*, vol. 16, pp. 1626–1633, 5 2021.

[37] S. M. B. Maezono, T. N. Poudel, and Y. R. Lee, "One-pot construction of sterically challenging and diverse polyarylphenols via transition-metal-free benzannulation and their potent in vitro antioxidant activity.," *Organic & biomolecular chemistry*, vol. 15, pp. 2052–2062, 3 2017.

[38] R. Aumann, "Organic syntheses via transition-metal complexes. part 58.

heptafulvenylcarbene complexes of chromium and tungsten. azaspiro(4) anellation to 1-metalla-1,3-dienes with isocyanides; displacement of ligands by pyridine or by thermolysis.," *ChemInform*, vol. 23, 8 1992.